Single-molecule analysis of cell surface dynamics in *Caenorhabditis elegans* embryos

François B Robin[1], William M McFadden[1,2], Baixue Yao[1] & Edwin M Munro[1,3,4]

We describe a general, versatile and minimally invasive method to image single molecules near the cell surface that can be applied to any GFP-tagged protein in *Caenorhabditis elegans* embryos. We exploited tunable expression via RNAi and a dynamically exchanging monomer pool to achieve fast, continuous single-molecule imaging at optimal densities with signal-to-noise ratios adequate for robust single-particle tracking (SPT). We introduce a method called smPReSS, single-molecule photobleaching relaxation to steady state, that infers exchange rates from quantitative analysis of single-molecule photobleaching kinetics without using SPT. Combining SPT and smPReSS allowed for spatially and temporally resolved measurements of protein mobility and exchange kinetics. We used these methods to (i) resolve distinct mobility states and spatial variation in exchange rates of the polarity protein PAR-6 and (ii) measure spatiotemporal modulation of actin filament assembly and disassembly. These methods offer a promising avenue to investigate dynamic mechanisms that pattern the embryonic cell surface.

Dynamic remodeling of the embryonic cell surface is essential for the control of cell polarity, division, shape change and movement during early development. This remodeling involves the local movement and exchange of proteins at the interface between the plasma membrane and the actin-rich cell cortex. Quantifying these processes *in vivo* remains a challenge. One promising approach is single-molecule imaging combined with SPT, which can yield quantitative measurements of local mobilities, binding states and exchange kinetics that are inaccessible with ensemble measurements[1–3]. Combining these approaches with genetic tools in a classical model organism could be a powerful way to investigate subcellular dynamics in embryonic cells.

One key impediment to performing such experiments has been the lack of simple and reliable methods for tunable and noninvasive labeling of target molecules. Optimal labeling densities are different for each target and must balance the need for high-density sampling of molecular behavior against practical requirements for accurate and unbiased single-molecule detection and tracking. Methods based on microinjection of fluorescently labeled probes[4,5] or transfection using crippled promoters[6–9] are cumbersome and inherently hard to optimize. Methods based on surface labeling of transmembrane proteins[10–13] may be easier to tune but cannot be generalized to intracellular targets. One approach for intracellular targets uses genetically encoded photoswitchable fluorescent protein fusions to create a renewable supply of single molecules[14–16].

Here we have described a simple, versatile and minimally invasive method for single-molecule imaging at the cell surface in *C. elegans* embryos that can be applied to any of the large and growing collection of transgenic strains expressing GFP-tagged fusion proteins[17]. We combined sequence-specific inhibition of GFP transgene expression with selective photobleaching and simple *in vivo* standards to achieve single-molecule densities of GFP fusions in the presence of normal levels of the endogenous protein. We exploited the intrinsic exchange dynamics of surface-associated proteins for long-term (>5,000 frames) sampling of single-molecule trajectories, at signal-to-noise ratios (SNRs), frame rates and densities that can be optimized to measure local mobility and turnover (per-molecule disappearance rates) for a given molecule. In particular, we showed how these data could be used to extract quantitative information about surface density and turnover. To demonstrate the power of this approach, we quantified spatiotemporal variations in mobility and turnover for the polarity protein PAR-6 and for actin filaments during cell division in the one-cell *C. elegans* embryo.

RESULTS

Imaging single molecules *in vivo*

In *C. elegans*, a 200-nm-thick eggshell[18,19] makes it difficult to image subsurface dynamics with true total-internal-reflection fluorescence (TIRF) optics. To overcome this, we used near-TIRF illumination[20], optimizing laser angle and intensity to achieve approximately even illumination across the field of view while maintaining adequate SNR for robust single-particle detection and tracking (**Fig. 1a**, **Supplementary Fig. 1** and Online Methods). For any given transgenic strain expressing GFP fused to a target protein, we used a two-step method to achieve densities of GFP-tagged proteins suitable for single-molecule imaging (**Fig. 1b**). First, we directed RNAi against the GFP sequence to selectively reduce maternal expression of the transgene, which
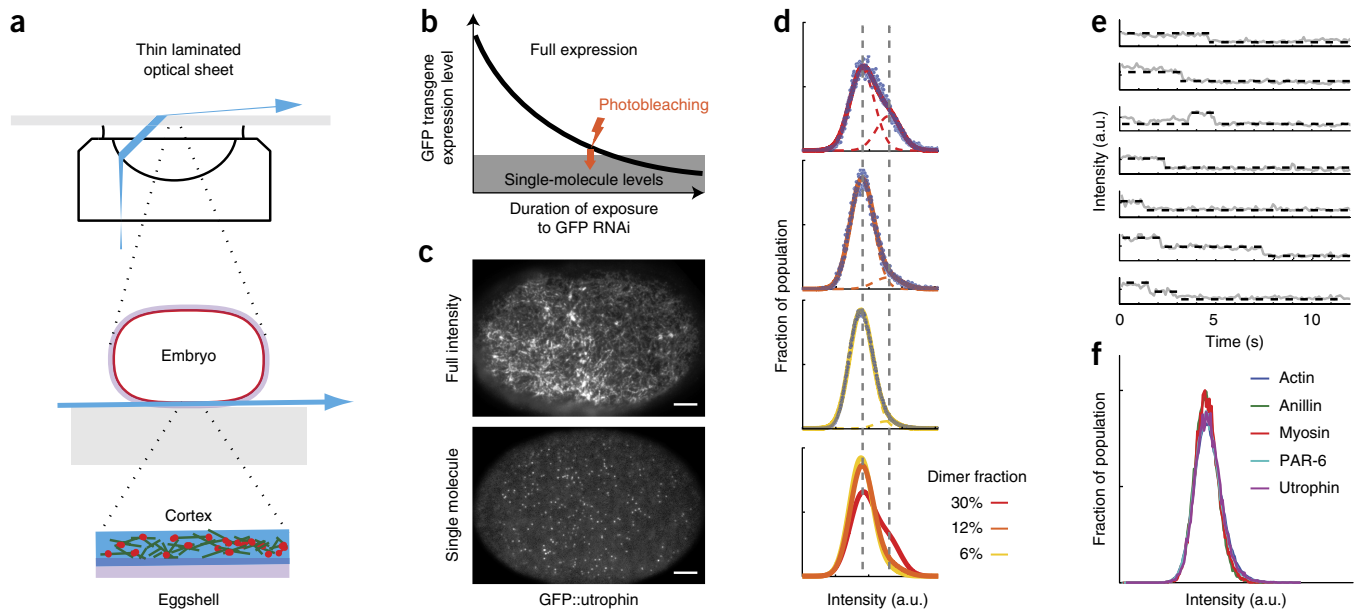
Figure 1 | Imaging single molecules at the cortex in living embryos. (**a**) Schematic of the near-TIRF imaging approach. The incident laser angle (top) at the coverglass-specimen interface is tuned to create a thin and narrowly inclined laminar sheet (blue) of laser light. At cellular (center) and subcellular (bottom) scales, the laminar sheet is nearly parallel to the coverslip-specimen interface and is thick enough to illuminate the entire cortex in the field of view. (**b**) Schematic of the approach to achieve single-molecule levels for any GFP-fusion strain in *C. elegans*, using a combination of RNAi and photobleaching. (**c**) Near-TIRF micrographs of a one-cell embryo expressing GFP∷utrophin, showing full intensity and single-molecule levels. Scale bars, 5 μm. (**d**) Distribution of intrinsic speckle intensities (average particle intensity – local average background; blue dots) in an embryo expressing GFP∷PAR-1 for a range of GFP levels. Fits to a sum of two Gaussians representing one- and two-molecule speckles are shown. The bottom panel compares directly all three previous panels. Images were obtained using identical imaging conditions. Gray dashed lines indicate average monomer (left) and dimer (right) intensities. (**e**) Fluorescence intensity changes upon photobleaching in an embryo expressing GFP∷actin. Multiple-step photobleaching can be readily detected at higher expression levels (bottom two panels). (**f**) Intrinsic speckle intensity at low particle densities across strains expressing GFP fusions to the indicated proteins. a.u., arbitrary units.

yielded presumably low levels of GFP-tagged protein in the presence of normal levels of endogenous protein. For more than a dozen strains tested, we could readily tune exposure times to obtain transgene expression levels at which diffraction-limited speckles, representing a few fluorophores, could be observed at the cell surface by near-TIRF microscopy (**Fig. 1c**). In a second step, we used photobleaching to further reduce speckle densities (the number of speckles per μm²) and mean speckle intensity toward single-molecule levels (**Fig. 1d**), with no adverse consequences for cell viability (Online Methods).

Next we established a general method to verify single-molecule levels for any GFP fusion strain that can be readily extended across labs and imaging platforms. We focused on the polarity maintenance phase in the one-cell embryo, a period of time late in the first cell cycle when the cell is stably polarized and the distributions of many surface proteins are essentially stationary. In a transgenic *C. elegans* strain expressing GFP fused with actin (GFP∷actin), we reduced transgene levels as above until the average intrinsic speckle intensity ($I_{int} = I_{speckle} - I_{background}$) reached a minimum value and the distribution of intensities was well fit by a single Gaussian (**Fig. 1d**). Then we imaged at high laser power such that speckle disappearance was predominantly due to photobleaching rather than disassembly. Under these conditions, the majority of disappearance events occurred in single steps, confirming that the minimum intensity speckles we observed corresponded to single GFP molecules (**Fig. 1e**). Strikingly, when we reduced expression in five other GFP fusion strains to minimize the mean speckle intensity, we measured speckle intensity

distributions during the polarity maintenance phase that were indistinguishable from one another and from those measured for GFP∷actin under the same imaging conditions (**Fig. 1f**). Moreover, by fitting multiple Gaussians (for 1, 2, … *N* fluorophores per particle) to the distribution of I_{int}, we could readily detect when more than 5% of speckles contained multiple fluorophores (**Fig. 1d** and **Supplementary Figs. 2** and **3a**). Thus, for any given strain, it is possible to pinpoint a characteristic speckle density below which a 'pure' population of single molecules can be reliably observed, which can subsequently be used to calibrate single-molecule imaging on other platforms.

Long-term single-molecule imaging of mobility and turnover
We sought to exploit the intrinsic exchange dynamics of surface-associated proteins to create a self-renewing pool of GFP-tagged single molecules at the cell surface that could be followed over time to measure mobility and turnover. To establish a kinetic basis for this approach, we consider a GFP-tagged protein that exchanges dynamically between the bulk cytoplasm and a region of the cell surface, which is observed by near-TIRF microscopy (**Fig. 2a**). The number of molecules $N(t)$ within this region over time is governed by

$$\frac{dN}{dt} = k_{app} - (k_{off} + k_{ph})N \qquad (1)$$

where k_{app} is an observable appearance rate that depends on the cytoplasmic concentration of GFP-tagged protein ($k_{app} = k_{on} \times Y$, where Y is the cytoplasmic concentration) and the nature of the

Figure 2 | Long-term sampling of single cell-surface molecules *in vivo*. (**a**) The basic kinetic principle: during imaging, the level of surface-associated proteins is set by a dynamic balance of appearance (binding or assembly) at an observable rate k_{app}, disappearance (unbinding or disassembly) at a per-molecule rate k_{off}, and photobleaching at a per-molecule rate k_{ph}. (**b**) Predicted response of an initially unobserved cell at steady state to a step change in illumination. For an infinite cytoplasmic pool, the surface density relaxes to a new illuminated steady state. For a finite cytoplasmic pool, fast relaxation is accompanied by a slower decay caused by irreversible photobleaching. (**c**) Fast relaxation to a quasi-stable density during illumination is rapidly reversed when the laser is turned off. (**d**) Biphasic response for GFP∷actin under illumination conditions that allow accurate single-molecule detection and tracking. Time from t = 30–450 s is discontinuous. (**e**) Surface density of GFP∷actin vs. time at various laser exposures, shown as a fraction of the initial unobserved density. Error bars, s.e.m. (n = 7, 9, 6, 7 embryos for laser exposures from low to high). (**f**) Estimates of per-molecule turnover (k_{off}) and photobleaching (k_{ph}) rates as a function of laser exposure. Error bars, s.d. (n = 12, 7, 8, 9, 7, 6, 7, 7 embryos, low to high laser exposure). Solid lines show a linear regression against the data. 100% laser power ≈ 1.6 µW µm^{-2}.
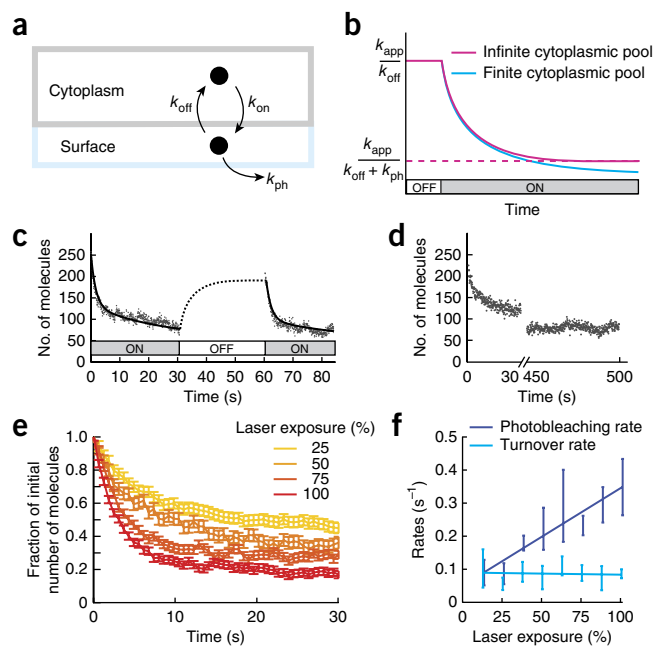

binding process. k_{off} and k_{ph} are pseudo-first-order rate constants such that $k_{off} \times N$ is the rate (in molecules per second) at which particles disappear owing to unbinding or disassembly, and $k_{ph} \times N$ is the rate (in molecules per second) at which they disappear owing to irreversible photobleaching (**Fig. 2a**). Prior to illumination, $k_{ph} = 0$ and the steady state density is $N_{ss} \approx k_{app}/k_{off}$. During illumination, k_{ph} becomes nonzero; if the cytoplasmic pool were infinite, the system would approach a new steady-state density given by $N_{ss}^{obs} = k_{app}/(k_{off} + k_{ph})$, which is a fixed fraction $f = k_{off}/(k_{off} + k_{ph})$ of the initial unobserved value (**Fig. 2b**). In practice, irreversible photobleaching will gradually deplete a finite cytoplasmic pool. A variant of the kinetic model that accounts for this depletion (Online Methods) predicts a biphasic response to the onset of illumination: a fast relaxation toward ~N_{ss}^{obs} followed by a slower decay toward 0, at a rate that depends on the photobleaching rate and the size of the cytoplasmic pool (**Fig. 2b** and **Supplementary Note 1**). For a given target molecule, k_{off} is fixed. However, k_{ph} depends on imaging conditions (i.e., the intensity and duty ratio of the laser illumination), and k_{app} can be adjusted by tuning the initial size of the GFP-tagged pool. Thus, co-tuning these factors should make it possible to target a desired density N_{ss}^{obs} at quasi-steady state for a range of imaging conditions.

To test this approach, we chose two representative strains that expressed GFP∷actin and PAR-6∷GFP, respectively. Actin monomers exchange dynamically with the cell surface through local filament assembly and disassembly, and on the basis of previous work, we expected GFP∷F-actin to be relatively immobile at the cell surface and to turn over in a few tens of seconds[21]. In contrast, fast-diffusing monomers of GFP∷G-actin should produce highly blurred images and thus escape detection under our imaging conditions[6]. PAR-6 is a conserved polarity protein that binds dynamically to sites on the plasma membrane[22–24], and recent fluorescence recovery after photobleaching (FRAP) measurements suggest that PAR-6 diffuses rapidly at the cell surface and dissociates very slowly[25], with an effective dissociation rate constant $k_{off} = 0.0054 \pm 0.005$ s^{-1} (±s.d. throughout). Focusing again on the polarity maintenance phase, we reduced densities to single-molecule levels, allowed the system to equilibrate unobserved and

then recorded data for a range of laser intensities and exposure times (**Fig. 2c–e** and **Supplementary Figs. 2** and **3b**). For both strains, we observed the predicted biphasic response to a step change in illumination: a rapid initial decrease in the number of molecules to a quasi-stable value followed by slower decay (**Fig. 2c,d**, **Supplementary Figs. 2** and **3a** and **Supplementary Video 1**). Notably, the initial decrease was reversed with equally rapid kinetics when the laser was turned off (**Fig. 2c**), a result confirming that the quasi-steady state is set by a dynamic balance of exchange and photobleaching. For both strains, we could therefore obtain robust estimates for effective dissociation and photobleaching rate constants k_{off} and k_{ph} by fitting the predicted biphasic kinetics to the change in single-molecule density over time; for each strain, we optimized fitting conditions by adjusting laser exposure (intensity and duty ratio; see below and **Supplementary Note 2**). As expected, estimates of k_{ph} varied linearly with laser exposure, whereas estimates of k_{off} remained fixed over a range of exposures (**Fig. 2f**). Our estimates of k_{off} for PAR-6 in the anterior cortex ($k_{off} = 0.0074 \pm 0.0007$ s^{-1}) are consistent with those previously obtained by FRAP ($k_{off} = 0.0054 \pm 0.005$ s^{-1}; ref. 25). We refer to this approach as smPReSS. Because smPReSS relies directly on counting single molecules, it is relatively insensitive to nonspecific fluorescence and can be applied at very low fluorophore densities that would be inaccessible for ensemble methods such as FRAP and its variants. Moreover, because smPReSS does not rely on particle tracking, it is insensitive to tracking errors.

Next we assessed the potential for long-term high-density sampling of single-molecule trajectories, as previously achieved with photoswitchable fluorophores. We set laser intensities to ensure that SNRs and frame rates were suitable for robust particle tracking using standard SPT algorithms and software[26,27] (**Supplementary Videos 1–3**, Online Methods and **Supplementary Table 1**). Under these conditions, we measured effective photobleaching rate constants $k_{ph} \approx 0.1$ s^{-1} for GFP∷actin and $k_{ph} \approx 0.3$ s^{-1} for PAR-6∷GFP, resulting in less than 30% loss in density over 5,000 frames (**Fig. 2d** and **Supplementary Figs. 2** and **3a**).

Figure 3 | Analysis of PAR-6∷GFP mobility.
(**a**) Distribution of track lengths for 30,558 tracks from $n = 5$ movies taken in one-cell embryos during the polarity maintenance phase. (**b**) Log-log plot of mean-square displacement (MSD) versus lag time ($\Delta\tau$) for all 177 tracks with length of ≥80 frames extracted from one of the movies. Traces have been assigned colors on the basis of slope (α). (**c**) Scatter plot of diffusion coefficient D versus exponent α, measured by fitting MSD = $4Dt^\alpha$ for the first ten lag times of the tracks shown in **b**. Color scheme same as in **b**. Inset shows two trajectories drawn from opposite ends of the scatter plot and indicated by colored circles. Scale bar, 1 µm. (**d**) Scatter plot for 177 trajectories obtained by simulating pure Brownian diffusion for ≥80 frames with $D = 0.15 \pm 0.05$ µm^2 s^{-1} and measuring D and α as in **c**. Note the close match to experimental data for $0.9 < \alpha < 1.2$ but the failure to match points for low D and α.
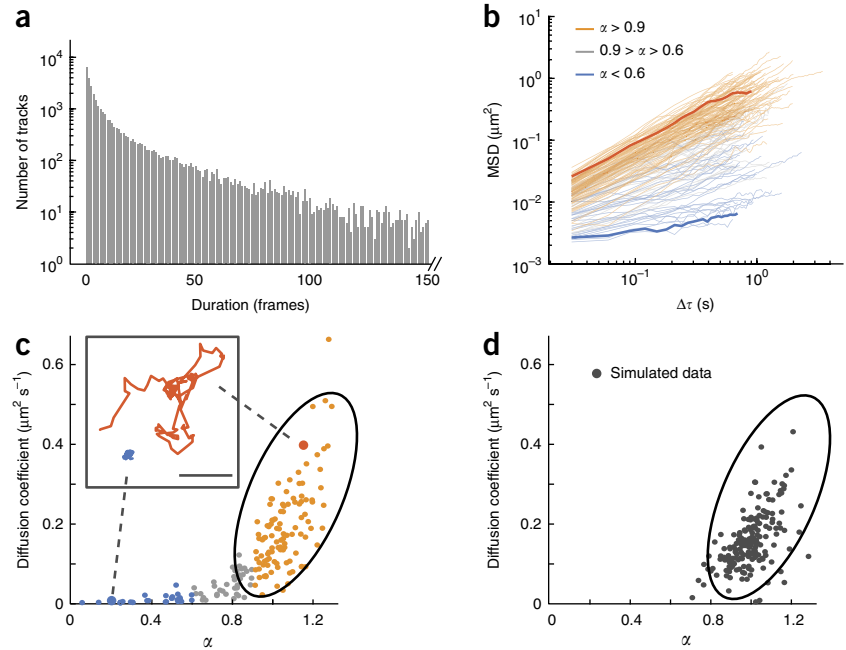
When we pre-tuned the initial size of the cytoplasmic pool to optimize quasi-stable densities toward maximal values consistent with robust SPT, we were able to recover for GFP∷actin (and PAR-6∷GFP, respectively) ~30,000 (~7,500) individual trajectories over the 5,000-frame interval, with an average duration of 35 (15) frames and ~5,000 (~250) trajectories lasting longer than 80 frames. We observed comparable results with several other strains expressing GFP fused with membrane or cortical proteins (GFP∷utrophin, GFP∷anillin, GFP∷PAR-1; data not shown).

In vivo SPT analysis of PAR-6 mobility
The ability to rapidly sample large numbers of individual trajectories makes it possible to analyze surface dynamics during brief windows of developmental time. To illustrate this, we tracked local movements of PAR-6∷GFP molecules at the cell surface during the maintenance phase in one-cell embryos. We measured mean-square displacement (MSD) versus lag time τ on 1,086 trajectories with lifetimes larger than 80 frames (**Fig. 3a,b**). Then we fit the first ten time points to MSD = $4Dt^\alpha$ to estimate the anomalous diffusion exponent α and a short-term diffusivity D. This analysis revealed at least two distinct mobility classes (**Fig. 3b,c** and **Supplementary Videos 1,4** and **5**). Approximately 43% of PAR-6 molecules underwent what appears to be simple diffusion, with $0.9 < \alpha < 1.2$ and short-term diffusivity $D = 0.17 \pm 0.10$ µm^2 s^{-1} (**Fig. 3b,c**), comparable to previous measurements by FRAP (0.28 ± 0.05 µm^2 s^{-1}; ref. 25). Another ~22% of PAR-6 molecules seemed to undergo slower subdiffusive motion, with $\alpha < 0.6$ and short-term $D = 0.008 \pm 0.008$ µm^2 s^{-1} (**Fig. 3b,c**). The remaining 35% of the tracks underwent intermediate behavior, with short-term $D = 0.057 \pm 0.032$ µm^2 s^{-1} for $0.6 \leq \alpha \leq 0.9$ (**Fig. 3b,c**). Simulating Brownian diffusion with diffusivities chosen randomly from the range $D = 0.15 \pm 0.05$ µm^2 s^{-1} and then analyzing trajectories as above reproduced a distribution of short-term D and α values very similar to the distribution observed for the subset of real particles with $0.9 < \alpha < 1.2$ (**Fig. 3d**). In contrast (and as expected), for no values of D did simulated Brownian diffusion reproduce the class of trajectories for $\alpha < 0.6$ observed for single molecules of PAR-6 (**Supplementary Fig. 4**).

These observations are consistent with previous studies documenting two populations of PAR-6, punctate and diffuse, with distinct localizations and genetic requirements, and which likely reflect different binding modes and binding partners for PAR-6 (ref. 22). Further analyses combining the sampling methods introduced here with, for example, Bayesian trajectory analysis[28,29] and genetic manipulation should yield further information about these different binding states and their regulation.

Measuring spatiotemporal variations in density/turnover
GFP-tagged proteins report not just on mobilities of the endogenous molecules but also on spatiotemporal variation in densities, appearance rates (k_{app}) and per-molecule turnover rates (k_{off}). In principle, k_{app} and k_{off} can be measured either directly from single-molecule trajectories or by smPReSS as described above. However, practical considerations constrained the choice of method as illustrated below.

Measuring spatial variation of PAR-6 turnover
PAR-6 is highly enriched at the anterior (versus posterior) cortex in polarized one-cell embryos. This difference is thought to be caused by more rapid dissociation of PAR-6 in the posterior[30]. Anterior-versus-posterior differences in dissociation rate cannot be detected by conventional FRAP analysis because the densities of PAR-6 in the posterior are too low. Furthermore, the photobleaching rates ($k_{ph} \approx 0.3$ s^{-1}) required for accurate particle tracking are ~40-fold higher than the dissociation rates ($k_{off} = 0.0074 \pm 0.0007$ s^{-1}) measured by smPReSS. Thus, resolving anterior-posterior differences in turnover by particle tracking would be difficult or impossible because photobleaching will dominate small differences in k_{off}. Instead, we exploited the tunability of our approach, setting laser exposure and image acquisition (100% laser, 30-ms exposure at 1-s intervals) to maintain accurate detection while reducing photobleaching rates to $k_{ph} \approx 0.005$. Under these conditions, smPReSS yielded robust estimates of k_{off} for anterior and posterior regions

Figure 4 | Analysis of actin dynamics in *nmy-2* RNAi embryos. (**a**) Near-TIRF micrographs of GFP∷actin during the polarity maintenance phase (top) and cleavage (bottom). (**b**) Measurements of the indicated turnover rates at the equator and poles during anaphase using tracking (left) or smPReSS (right). Schematic indicates the equatorial (dashed box) and polar (solid boxes) regions in which the measurements were made. For tracking, the sum of k_{off} and k_{ph} is displayed; for smPReSS, the values for k_{ph} and k_{off} are stacked. (**c**–**e**) Spatial variation in actin density and turnover kinetics during maintenance phase and cleavage measured by tracking and binned along the antero-posterior axis. (**c**) Cortical density. (**d**) Polymerization rate. (**e**) Depolymerization rate (instantaneous disappearance rate minus estimated photobleaching rate). In **b**–**e**, error bars indicate cell-to-cell s.e.m. (*n* = 7 embryos, maintenance, and *n* = 16 embryos, cleavage). Scale bar, 5 μm.

(k_{off}^{ant} = 0.0074 ± 0.0007 s⁻¹, k_{off}^{post} = 0.0092 ± 0.0020 s⁻¹). In combination with measurements of relative density (N_{ant}/N_{post} = 9.0 ± 1.4), this allowed us to infer relative values for k_{app} ($k_{app}^{ant}/k_{app}^{post}$ = 7.2 ± 2.0). Interestingly, our results suggest that the majority of the anterior-posterior difference in density is due to differences in recruitment rates, which is consistent with the enrichment of several known binding partners for PAR-6 (CDC-42 and PAR-3) at the anterior[22,31].

Modulation of actin assembly/turnover during cell division

We measured spatiotemporal modulation of actin assembly and disassembly during the first cell division in the *C. elegans* embryo (**Fig. 4a** and **Supplementary Videos 2** and **3**). Both actin assembly and disassembly are thought to be modulated during cytokinesis[32], but their relative contributions to actin filament accumulation are not well understood. We performed these experiments in embryos depleted of nonmuscle myosin II to remove the confounding effects of surface deformations and flow and to remove myosin-dependent effects on turnover[33,34]. We verified strong depletion of myosin II by the complete failure of cytokinesis and a complete absence of local surface deformation and cortical flow during early anaphase. In the case of GFP∷actin, the turnover rates measured by smPReSS (k_{off} ≈ 0.1 s⁻¹) were similar to the photobleaching rates (k_{ph} ≈ 0.1 s⁻¹) required for accurate particle tracking and agreed well with estimates of k_{off} from particle tracking (**Fig. 4b** and **Supplementary Fig. 5**), suggesting that in this case, we could use SPT to measure spatiotemporal variations in turnover, with the smPReSS measurements of k_{ph} used to correct for photobleaching. We measured roughly uniform values for k_{app} and k_{off} along the anterior-posterior axis during maintenance phase (**Fig. 4c**–**e**), a result consistent with a lack of cortical asymmetry at this stage in myosin-depleted embryos (data not shown). During the transition into anaphase, when the contractile ring normally assembles, we observed a net increase in actin density at the equator as anticipated, and we also observed a net decrease at the poles (**Fig. 4a,c**). Surprisingly, these changes involved strong modulation of both filament assembly and disassembly (**Fig. 4d,e**). The equatorial increase was associated with a small increase in assembly rate and a larger decrease in turnover, whereas the polar decrease in density was associated with both a decrease in assembly and an increase in turnover. Thus, our ability to simultaneously resolve assembly, disassembly and density revealed an unappreciated dimension to the control of cortical microfilaments during cell division.
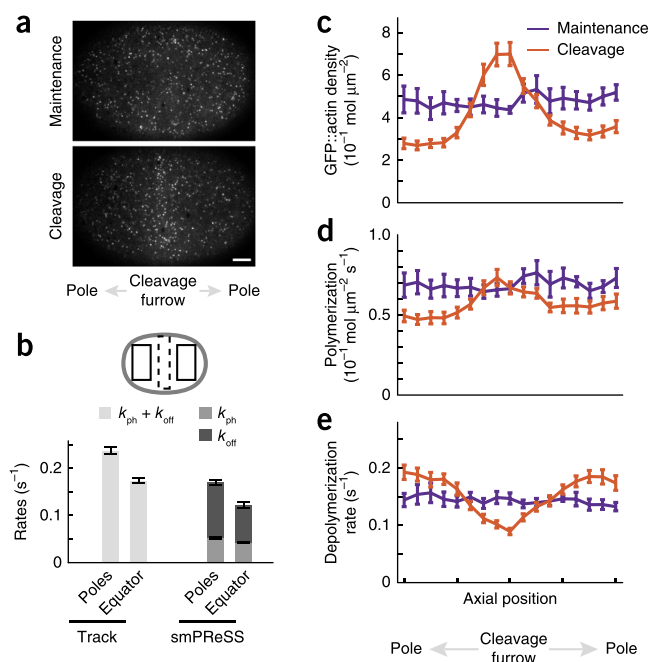
DISCUSSION

Here we described a simple and tunable method to monitor single-molecule mobility and exchange dynamics at the cell surface in embryonic cells of *C. elegans*. By tuning the size of the GFP-tagged pool and photobleaching rates, we obtained continuous long-term sampling of single-molecule trajectories, at densities and track lengths that are limited mainly by the photostability of GFP and by well-known constraints on the accurate detection and tracking of single molecules. We focused here on single-molecule imaging and analysis. However, brighter (multimolecule) speckles may be optimal for some analyses[35] and can be readily achieved through a slightly different tuning of the cytoplasmic pool. Our approach is minimally invasive because it relies on sampling low levels of GFP fusions, with no detectable phototoxicity even at very high laser power. A previous method relied on reversible binding of fluorescently tagged extracellular ligands to sample cell-surface receptors[36]. Here we rely on the intrinsic exchange of GFP fusion proteins between the cytoplasm and the cell surface to sample the dynamics of a large class of intracellular proteins. No additional methods or reagents are required to target fluorophores to the protein of interest, and the method can be readily implemented by anyone with access to a TIRF microscope equipped for GFP excitation and a sufficiently sensitive camera (for example, an electron-multiplying charge-coupled device (EMCCD)). Our approach thus leverages the large collection of existing fusion strains in *C. elegans*[17], plus recently developed methods for the rapid production of new strains by genome editing[37], and can be readily combined with any of the large arsenal of molecular genetics tools available for this model organism.

Our approach is immediately compatible with a growing array of SPT-based tools to analyze local heterogeneity and spatiotemporal variation in mobility and binding states[28,29]. Under conditions in which photobleaching rates do not dominate turnover (for example, low mobility and fast turnover as for GFP∷actin), it is possible to measure spatiotemporal variation in turnover directly from single-particle trajectories. As an alternative, we introduced

a method called smPReSS that estimates bulk turnover rates by fitting single-molecule counts over time to kinetic exchange models. smPReSS relies only on single-molecule detection and thus is insensitive to particle tracking errors. As illustrated by our analysis of PAR-6 turnover, smPReSS can be tuned to measure turnover rates under conditions that are inaccessible to SPT analysis or to ensemble-based measurements such as FRAP and its variants. A key assumption underlying both approaches is that the kinetics remain stationary during the time it takes to measure them; the validity of this assumption must be assessed on a case-by-case basis.

Finally, although we developed and optimized the methods described here for use in *C. elegans*, sequence-specific inhibition of GFP expression and the use of intrinsic turnover to sample single-molecule dynamics could be implemented in other organisms and cell types. Combining these methods with molecular genetic tools already available offers a promising new avenue to study cell surface dynamics in developing embryos.

METHODS

Methods and any associated references are available in the online version of the paper.

Note: Any Supplementary Information and Source Data files are available in the online version of the paper.

AUTHOR CONTRIBUTIONS

E.M.M. conceived the imaging approach and provided overall guidance. F.B.R. conceived and developed the smPReSS approach and, with E.M.M., developed the tracking-based turnover analysis. F.B.R. and W.M.M. acquired the data for actin; B.Y. and F.B.R. acquired the data for PAR-6; W.M.M., F.B.R. and B.Y. performed the nonlinear fitting; E.M.M., F.B.R., B.Y. and W.M.M. developed and performed the mobility analysis. F.B.R. performed the tracking-based turnover analysis, and F.B.R., W.M.M., B.Y. and E.M.M. made the figures. E.M.M. and F.B.R. wrote the text.

Reprints and permissions information is available online at http://www.nature.com/reprints/index.html.

1. Lord, S.J., Lee, H.L. & Moerner, W.E. Single-molecule spectroscopy and imaging of biomolecules in living cells. *Anal. Chem.* **82**, 2192–2203 (2010).
2. Xia, T., Li, N. & Fang, X. Single-molecule fluorescence imaging in living cells. *Annu. Rev. Phys. Chem.* **64**, 459–480 (2013).
3. Sako, Y. *et al.* Live cell single-molecule detection in systems biology. *Wiley Interdiscip. Rev. Syst. Biol. Med.* **4**, 183–192 (2012).
4. Waterman-Storer, C.M., Desai, A., Bulinski, J.C. & Salmon, E.D. Fluorescent speckle microscopy, a method to visualize the dynamics of protein assemblies in living cells. *Curr. Biol.* **8**, 1227–1230 (1998).
5. Ponti, A., Machacek, M., Gupton, S.L., Waterman-Storer, C.M. & Danuser, G. Two distinct actin networks drive the protrusion of migrating cells. *Science* **305**, 1782–1786 (2004).
6. Watanabe, N. & Mitchison, T.J. Single-molecule speckle analysis of actin filament turnover in lamellipodia. *Science* **295**, 1083–1086 (2002).
7. Douglass, A.D. & Vale, R.D. Single-molecule imaging of fluorescent proteins. *Methods Cell Biol.* **85**, 113–125 (2008).
8. Douglass, A.D. & Vale, R.D. Single-molecule microscopy reveals plasma membrane microdomains created by protein-protein networks that exclude or trap signaling molecules in T cells. *Cell* **121**, 937–950 (2005).
9. Millius, A., Watanabe, N. & Weiner, O.D. Diffusion, capture and recycling of SCAR/WAVE and Arp2/3 complexes observed in cells by single-molecule imaging. *J. Cell Sci.* **125**, 1165–1176 (2012).
10. Ueda, M., Sako, Y., Tanaka, T., Devreotes, P. & Yanagida, T. Single-molecule analysis of chemotactic signaling in *Dictyostelium* cells. *Science* **294**, 864–867 (2001).
11. Uyemura, T., Takagi, H., Yanagida, T. & Sako, Y. Single-molecule analysis of epidermal growth factor signaling that leads to ultrasensitive calcium response. *Biophys. J.* **88**, 3720–3730 (2005).
12. Jaqaman, K. *et al.* Cytoskeletal control of CD36 diffusion promotes its receptor and signaling function. *Cell* **146**, 593–606 (2011).
13. Giannone, G. *et al.* Dynamic superresolution imaging of endogenous proteins on living cells at ultra-high density. *Biophys. J.* **99**, 1303–1310 (2010).
14. Manley, S. *et al.* High-density mapping of single-molecule trajectories with photoactivated localization microscopy. *Nat. Methods* **5**, 155–157 (2008).
15. Burnette, D.T. *et al.* A role for actin arcs in the leading-edge advance of migrating cells. *Nat. Cell Biol.* **13**, 371–381 (2011).
16. Niu, L. & Yu, J. Investigating intracellular dynamics of FtsZ cytoskeleton with photoactivation single-molecule tracking. *Biophys. J.* **95**, 2009–2016 (2008).
17. Sarov, M. *et al.* A genome-scale resource for *in vivo* tag-based protein function exploration in *C. elegans*. *Cell* **150**, 855–866 (2012).
18. Bird, A.F. & Bird, J. *The Structure of Nematodes* 2nd edn. (Academic Press, 1991).
19. Rappleye, C.A., Paredez, A.R., Smith, C.W., McDonald, K.L. & Aroian, R.V. The coronin-like protein POD-1 is required for anterior-posterior axis formation and cellular architecture in the nematode *Caenorhabditis elegans*. *Genes Dev.* **13**, 2838–2851 (1999).
20. Tokunaga, M., Imamoto, N. & Sakata-Sogawa, K. Highly inclined thin illumination enables clear single-molecule imaging in cells. *Nat. Methods* **5**, 159–161 (2008).
21. Salbreux, G., Charras, G. & Paluch, E. Actin cortex mechanics and cellular morphogenesis. *Trends Cell Biol.* **22**, 536–545 (2012).
22. Beers, M. & Kemphues, K. Depletion of the co-chaperone CDC-37 reveals two modes of PAR-6 cortical association in *C. elegans* embryos. *Development* **133**, 3745–3754 (2006).
23. Nakayama, Y. *et al.* Dynamin participates in the maintenance of anterior polarity in the *Caenorhabditis elegans* embryo. *Dev. Cell* **16**, 889–900 (2009).
24. Cheeks, R.J. *et al.* *C. elegans* PAR proteins function by mobilizing and stabilizing asymmetrically localized protein complexes. *Curr. Biol.* **14**, 851–862 (2004).
25. Goehring, N.W., Hoege, C., Grill, S.W. & Hyman, A.A. PAR proteins diffuse freely across the anterior-posterior boundary in polarized *C. elegans* embryos. *J. Cell Biol.* **193**, 583–594 (2011).
26. Pelletier, V., Gal, N., Fournier, P. & Kilfoil, M.L. Microrheology of microtubule solutions and actin-microtubule composite networks. *Phys. Rev. Lett.* **102**, 188303 (2009).
27. Jaqaman, K. *et al.* Robust single-particle tracking in live-cell time-lapse sequences. *Nat. Methods* **5**, 695–702 (2008).
28. Monnier, N. *et al.* Bayesian approach to MSD-based analysis of particle motion in live cells. *Biophys. J.* **103**, 616–626 (2012).
29. Persson, F., Lindén, M., Unoson, C. & Elf, J. Extracting intracellular diffusive states and transition rates from single-molecule tracking data. *Nat. Methods* **10**, 265–269 (2013).
30. Hoege, C. & Hyman, A.A. Principles of PAR polarity in *Caenorhabditis elegans* embryos. *Nat. Rev. Mol. Cell Biol.* **14**, 315–322 (2013).
31. Kumfer, K.T. *et al.* CGEF-1 and CHIN-1 regulate CDC-42 activity during asymmetric division in the *Caenorhabditis elegans* embryo. *Mol. Biol. Cell* **21**, 266–277 (2010).
32. Pollard, T.D. Mechanics of cytokinesis in eukaryotes. *Curr. Opin. Cell Biol.* **22**, 50–56 (2010).
33. Guha, M., Zhou, M. & Wang, Y.L. Cortical actin turnover during cytokinesis requires myosin II. *Curr. Biol.* **15**, 732–736 (2005).
34. Murthy, K. & Wadsworth, P. Myosin II-dependent localization and dynamics of F-actin during cytokinesis. *Curr. Biol.* **15**, 724–731 (2005).
35. Danuser, G. & Waterman-Storer, C.M. Quantitative fluorescent speckle microscopy of cytoskeleton dynamics. *Annu. Rev. Biophys. Biomol. Struct.* **35**, 361–387 (2006).
36. Giannone, G. *et al.* Dynamic superresolution imaging of endogenous proteins on living cells at ultra-high density. *Biophys. J.* **99**, 1303–1310 (2010).
37. Dickinson, D.J., Ward, J.D., Reiner, D.J. & Goldstein, B. Engineering the *Caenorhabditis* genome using Cas9-triggered homologous recombination. *Nat. Methods* **10**, 1028–1034 (2013).

ONLINE METHODS

C. elegans **culture and strains.** We cultured *C. elegans* strains under standard conditions[38]. The GFP fusion strains used in this study are GFP∷actin, JH1541, *unc-119*(*ed4*);pJH7.03 [*unc-119*; *pie-1*:GFP:actin∷*pie-1* 3′ UTR] (courtesy of G. Seydoux); GFP∷PAR-1, JH1734, *unc-119*(*ed3*); axIs1245[pAC2.01: *pie-1*∷ GFP∷*par-1*∷*pie-1* 3′ UTR] (ref. 39); GFP∷ANI-1, OD38, *unc-119* (*ed3*) III; ltIs28 [pASM14; *pie-1*∷GFP-TEV-STAG∷*ani-1*∷*pie-1* 3′ UTR; *unc-119*(+)] (ref. 40); GFP∷utrophin, MG589, mgSi3[*Cb-unc-119*(+) *pie-1*∷GFP∷utrophin∷*pie-1* 3′ UTR] II (3); PAR-6∷ GFP, FT17, xnIs3[*par-6*∷*par-6*∷GFP + *unc-119*(+)] (ref. 41); NMY-2∷GFP, JJ1667: *unc-119*(*ed3*) III (ref. 42); zuIs115 [pKG47: *nmy-2*∷GFP; *unc-119*(+)] I (courtesy of J. Nance).

RNA interference. We performed RNAi using the feeding method[43]. Bacteria targeting *nmy-2* were obtained from the feeding library of Kamath *et al.*[44]. The L4417 plasmid targeting the entire GFP sequence (generated by the Fire lab and available at http://www.addgene.org/1649/) was transformed into HT115(DE3) bacteria. Bacterial cultures for feeding were grown for 10–12 h and then induced on standard nematode nutritional growth media plates containing 50 µg/ml ampicillin and 1 mM IPTG for 16–24 h at 20–25 °C. For *nmy-2*(RNAi), L4 stage larvae were placed on feeding plates for 20–28 h before imaging.

One potential issue with these experiments is that RNAi directed against GFP in strains expressing GFP fused to a given protein could lead to depletion of its endogenous counterpart through a transitive RNAi effect[45,46]. The transitive effect is directional, affecting C-terminal fusions only; because the PAR-6∷ GFP strain used in this study is a C-terminal fusion, there was a possibility that transitive RNAi could bias our results. However, in every PAR-6∷GFP embryo that we examined, we observed strong anterior-posterior patterning of residual PAR-6∷GFP when it was reduced to single-molecule level, and these embryos divided asymmetrically with a normal cleavage furrow position. To further verify the absence of a transitive depletion effect, we placed L4 hermaphrodites onto GFP RNAi plates for 24 h, transferred them as single worms to new GFP RNAi plates for >48 h and then scored their progeny for survival. In all cases (10/10), the worms made roughly normal brood sizes, and 100% of their eggs hatched into L1 larvae.

Imaging conditions. We dissected one-cell embryos from gravid hermaphrodites and mounted them under #1.5 22-mm square coverslips in 3.5 µl of standard egg buffer (118 mM NaCl, 40 mM KCl, 3.4 mM CaCl2, 3.4 mM MgCl2, 5 mM HEPES, pH 7.4) containing ~100 uniformly sized polystyrene beads (15.6 ± 0.03 µm diameter, Bangs labs, #NT29N) to achieve uniform compression of the embryo surface across experiments.

We performed near-TIRF imaging on an inverted Nikon Ti-E microscope, equipped with a motorized TIRF illuminator, a CFI Apo 1.45–numerical aperture (NA)/100× oil-immersion TIRF objective (Nikon) and a Ti-ND6-PFS Perfect Focus unit. Laser illumination at 488 nm from a 50-mW solid-state sapphire laser (Coherent) was delivered by fiber optics to the TIRF illuminator. Images were magnified by 1.5× and collected on an Andor iXon3 897 EMCCD camera, yielding a pixel size of 107 nm.

We controlled laser illumination angle and intensity and image acquisition using MetaMorph software (Molecular Devices).

For all experiments, we set the laser illumination angle to a standard value that was chosen empirically to approximately maximize signal intensity while maintaining approximately even illumination across the field of view. For SPT experiments, we collected images in streaming mode with continuous illumination at 20–100% laser intensity (100% ≈ 1.6 µW µm^{-2}) with 30- to 100-ms exposures to achieve frame rates of 10–30 frames/s. In some experiments we varied the duty ratio of laser exposure by operating the system in time-lapse mode with fixed laser intensity and exposure time and varied the interval between exposures to systematically vary photobleaching rates.

Tuning GFP levels to achieve single-molecule densities. The quasi-steady-state densities observed during imaging depend on the initial (unobserved) densities, photobleaching rates and the intrinsic exchange kinetics of the target molecule (see main text and below). Thus we determined the appropriate initial densities empirically for a given strain and experiment. We achieved these initial densities in two steps. First, we used RNAi directed against the GFP sequence to deplete the maternal pool of GFP-tagged protein. RNAi against maternal proteins typically yields an exponential decrease in the maternal protein with time of exposure[47]. We controlled the degree of depletion by synchronizing larvae and sampling embryos at different times after the initiation of feeding to identify times at which discrete diffraction-limited speckles were observed at the cell surface. The optimal time varied from 12–36 h depending on transgene expression levels and relative abundance at the cell surface vs. cytoplasm, but it was relatively consistent across experiments for a given strain. In a second step, we further 'pre-tuned' GFP densities using pulses of <10 s in epi-illumination mode at 100% laser power (~1.6 µW µm^{-2}) until adequate density was reached.

Assessing potential effects of compression, laser exposure and GFP tagging. Using photobleaching to reduce GFP-tagged protein levels from full to single-molecule levels in one step resulted in arrested development. However, the laser exposure required to fine-tune densities by photobleaching, or that occurring during single-molecule imaging, did not cause embryos to arrest. In all of our single-molecule imaging experiments, we verified that embryos initiated and completed cytokinesis with normal timing (PAR-6∷GFP; 18/18) or, in the case of myosin-depleted embryos expressing GFP∷actin, attempted cytokinesis with normal timing. To further confirm a lack of phototoxicity, we imaged embryos expressing single-molecule levels of PAR-6∷GFP at 100% laser power continuously for 150 s and then scored for (i) normal progression to the four-cell stage and (ii) hatching. We performed this experiment under two mounting conditions: with embryos mounted under coverslips supported by ~15-µm beads as in most of our experiments, and with embryos mounted on agar pads, which are slightly less compressed. We found that 100% of the embryos imaged with glass beads progressed normally to the four-cell stage, but only 1/10 actually hatched. In contrast, we found that 10/10 embryos imaged on agar pads hatched as normal L1 larvae. Because the laser exposure is approximately the same in both mounting conditions, we conclude that the failure of embryos imaged with glass beads to hatch is not due to phototoxicity *per se* but rather to the greater compression of embryos mounted with 15-µm glass beads, which may affect the physical

relationship between blastomeres at later stages and thus signaling processes that underlie cell fate determination. It remains a possibility that the dynamics observed in compressed embryos are slightly altered relative to uncompressed embryos, and this should be taken into account when interpreting results obtained using this method.

Another potential issue to consider is the effects of the GFP tag itself on the observed single-molecule dynamics. In the case of PAR-6∷GFP, we used a transgene that has been shown to rescue a null mutation in *par-6*, suggesting that the effects on observed dynamics is minimal. We have not verified functional rescue by GFP∷actin, and thus the turnover rates measured with this probe may not be identical to the endogenous turnover rates for F-actin. This should have no bearing on the validity or accuracy of the methods we report here, and it should not alter our qualitative conclusions that both F-actin assembly and turnover are modulated spatially and temporally during cytokinesis, but it may affect the quantitative differences we report, and these should therefore be interpreted with appropriate care.

Verifying single-molecule levels. Following Tokunaga *et al.*[20], we defined the intrinsic speckle intensity as the averaged intensity around the centroid of the particle over a 2-pixel radius minus the averaged background in a surrounding 2-pixel-wide region. To measure the mean and s.d. of the intrinsic intensity for single molecules (I_{mono} and σ_{mono}, respectively), we reduced GFP densities until the distribution of intrinsic speckle intensities no longer changed, and then we fit the distribution to a pure Gaussian. To estimate the distribution of speckle sizes (no. of GFP molecules per speckle) at higher densities as in **Figure 1f** and **Supplementary Figure 3a**, we fit the distribution of intrinsic speckle intensities to a sum of n Gaussians

$$G = \sum_{k=1}^{n} w_k G(I_k, \sigma_k)$$

where $G(I_k, \sigma_k)$ is a pure Gaussian with mean $I_k = I_{mono} \times k$ and s.d. $\sigma_k = \sigma_{mono} \times \sqrt{k}$. We found that $n = 3$ was sufficient to obtain good fits over the range of densities shown in **Figure 1f** and **Supplementary Figure 3a**. We performed all fits using Matlab's built-in fitting functions.

Single-molecule detection and tracking. We initially tested two different publicly available Matlab software packages for single-particle detection and tracking: the Kilfoil (http://people.umass.edu/kilfoil/downloads.html) implementation of the Crocker-Grier algorithm[26,48] and u-track[27] (http://lccb.hms.harvard.edu/software.html). In initial tests, both methods yielded very similar results for particle detection and tracking under the imaging conditions used here (average SNR ≈ 5; single-molecule densities such that trajectory mergers and splits are exceedingly rare; see **Supplementary Table 1**). Because the Kilfoil implementation of the Crocker-Grier method is substantially faster, we used it for all the analyses reported here.

In brief, the Crocker-Grier method localizes particles to subpixel resolution in individual frames by fitting local intensity peaks to a Gaussian point spread function. The two key detection parameters—peak and mean intensity of the candidate particles—are adjusted empirically for given imaging conditions using a graphical user interface. The particles are then linked frame to frame by minimizing the global displacement across all particles, given a user-chosen cutoff value for maximum particle displacement. A second parameter, the gap size, allows the possibility of ignoring 'gaps' in a trajectory due to transient failures to detect particles. These transient failures occur mainly because motion blur causes the particle intensity to fall transiently below the detection threshold. We infer this because, under identical imaging conditions and using identical detection parameters, slow-moving PAR-6∷GFP molecules (the 'subdiffusive' class in **Figure 3**) almost never fell below the detection threshold (see **Supplementary Video 5**), whereas fast-diffusing PAR-6∷GFP particles frequently escaped detection (see **Supplementary Video 4**).

For PAR-6∷GFP, which can be highly mobile and thus subject to motion blur (compare **Supplementary Videos 4** and **5**, which show fast- and slow-moving PAR-6∷GFP molecules), we used a cutoff value $r = 5$ and a gap size of seven frames, yielding a maximum gap time of $t_{gap} = 231$ ms. For these values, the probability of a molecule diffusing farther than r after a time t_{gap}

$$p(r, \Delta t) = 1 - e^{-r^2/4D\Delta t}$$

(ref. 49) was less than 0.05, and the maximum allowed jump of 5 pixels was nearly an order of magnitude less than the average distance between single molecules (~40 pixels; see **Supplementary Table 1**), ensuring that false gap closures are extremely rare.

For GFP∷actin, we used a maximum step-size cutoff value of 3 pixels and an allowable gap size of zero frames to perform the tracking shown in **Supplementary Table 1**. For the data shown in **Figure 4**, to further improve tracking for estimates of turnover by SPT, we preaveraged ten frames before the initial detection step and then performed tracking on the averaged data, again with a step size cutoff of 3 pixels and a gap size of 0. Allowing gap sizes of 1 or 2 in the analysis of the time-averaged data resulted in 18% (gap size = 1) and 25% (gap size = 2) of trajectories with reconnection events, suggesting that as many as 25% of the appearance and disappearance events counted in the analysis with gap size = 0 could be false. In principle, this could result in as much as a 25% overestimate of the absolute value of k_{off}. However, the fraction of trajectories with gaps was very similar at different axial positions (see **Supplementary Fig. 5**), suggesting that failures to detect some gap closures will have minimal impact on the relative values we report in **Figure 4**.

We measured an upper bound on the axial (1D) localization precision by tracking GFP∷utrophin molecules in embryos arrested in meiosis. Under these conditions, GFP∷utrophin is bound to a highly immobile network of cortical microfilaments, and thus measuring the amplitude of position fluctuations should yield an upper bound on the axial localization precision for a probe that has the same SNR as those used in our analysis of actin and PAR-6 dynamics. Following Huang *et al.*[50], we tracked each GFP molecule until it disappeared, resulting in iterative localization of 4,784 molecules. Then we aligned x and y particle positions from each track by their centers of mass to generate distributions of x and y position fluctuations, which we fit to a Gaussian function, yielding an s.d. of 24 ± 1 nm in x and y (**Supplementary Fig. 6**).

Generation of simulated trajectories for comparison to PAR-6 data. We simulated Brownian diffusion for a set of 177 particles with track

lengths matching those for the 177 trajectories shown in **Figure 3b,c**. For each trajectory, we selected at random a series of Brownian steps, with mean size $<x> = 4Dt$, where $t = 33$ ms was the interval between frames for the real data. Then we fit $MSD = 4Dt^{\alpha}$ for the first ten lag times to obtain 'estimates' for short-term diffusivity and anomalous diffusion exponent α. For the data shown in **Supplementary Figure 4**, we used a single value of D for all simulated particles, and we varied D from 0.1 to 0.6. For the simulated data shown in **Figure 3d**, we assigned a normally distributed diffusion coefficient to each simulated particle such that $D_{sim} \rightarrow N(0.15, 0.05)$.

38. Brenner, S. The genetics of *Caenorhabditis elegans*. *Genetics* **77**, 71–94 (1974).
39. Motegi, F. *et al.* Microtubules induce self-organization of polarized PAR domains in *Caenorhabditis elegans* zygotes. *Nat. Cell Biol.* **13**, 1361–1367 (2011).
40. Tse, Y.C. *et al.* RhoA activation during polarization and cytokinesis of the early *Caenorhabditis elegans* embryo is differentially dependent on NOP-1 and CYK-4. *Mol. Biol. Cell* **23**, 4020–4031 (2012).
41. Totong, R., Achilleos, A. & Nance, J. PAR-6 is required for junction formation but not apicobasal polarization in *C. elegans* embryonic epithelial cells. *Development* **134**, 1259–1268 (2007).
42. Munro, E., Nance, J. & Priess, J.R. Cortical flows powered by asymmetrical contraction transport PAR proteins to establish and maintain anterior-posterior polarity in the early *C. elegans* embryo. *Dev. Cell* **7**, 413–424 (2004).
43. Timmons, L. & Fire, A. Specific interference by ingested dsRNA. *Nature* **395**, 854 (1998).
44. Kamath, R.S. *et al.* Systematic functional analysis of the *Caenorhabditis elegans* genome using RNAi. *Nature* **421**, 231–237 (2003).
45. Sijen, T. *et al.* On the role of RNA amplification in dsRNA-triggered gene silencing. *Cell* **107**, 465–476 (2001).
46. Alder, M.N., Dames, S., Gaudet, J. & Mango, S.E. Gene silencing in *Caenorhabditis elegans* by transitive RNA interference. *RNA* **9**, 25–32 (2003).
47. Oegema, K. & Hyman, A.A. in *WormBook* (ed. The *C. elegans* Research Community) doi:10.1895/wormbook.1.72.1 (2006).
48. Crocker, J.C. & Grier, D.G. Methods of digital video microscopy for colloidal studies. *J. Colloid Interface Sci.* **179**, 298–310 (1996).
49. Saxton, M.J. Lateral diffusion in an archipelago. *Biophys. J.* **64**, 1766–1780 (1993).
50. Huang, B., Wang, W., Bates, M. & Zhuang, X. Three-dimensional super-resolution imaging by stochastic optical reconstruction microscopy. *Science* **319**, 810–813 (2008).
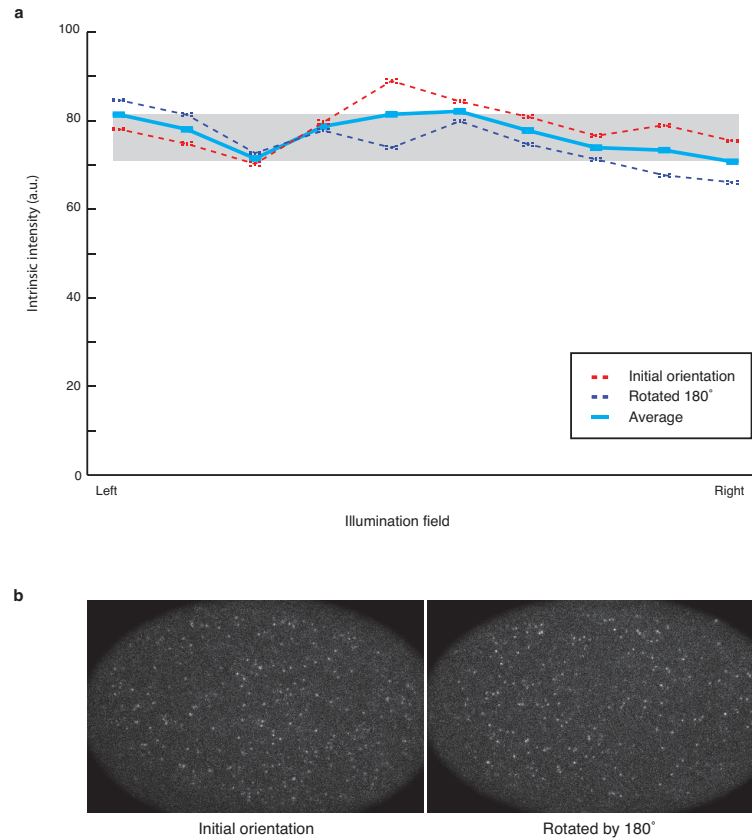
High-density single-molecule analysis of cell surface dynamics
in *C. elegans* embryos

Francois B. Robin, William M. McFadden, Baixue Yao and Edwin M. Munro

Supplementary materials

**Supplementary Figure 1.** Near-homogeneity of the illumination field.

(a) Plot of the average intrinsic intensity vs axial position, measured across the field of illumination in a GFP::Utrophin embryo during maintenance phase. We imaged the embryo for 2000 frames, rotated it by 180 degrees and then imaged for another 2000 frames. Graph shows the first 2000 frames in the initial orientation, second 2000 frames rotated by 180° and all 4000 frames averaged. Error bars indicate the standard error of the mean (n > 20 000 detections for each bin). Image acquistion was performed using 100% laser intensity, 30 ms exposure time and the same laser angle as in all other experiments.

(b) Single frames displaying the intensity of speckles in both orientation.

Supplementary Figure 2. Rapid decay to quasi-steady state in GFP::Actin embryos.
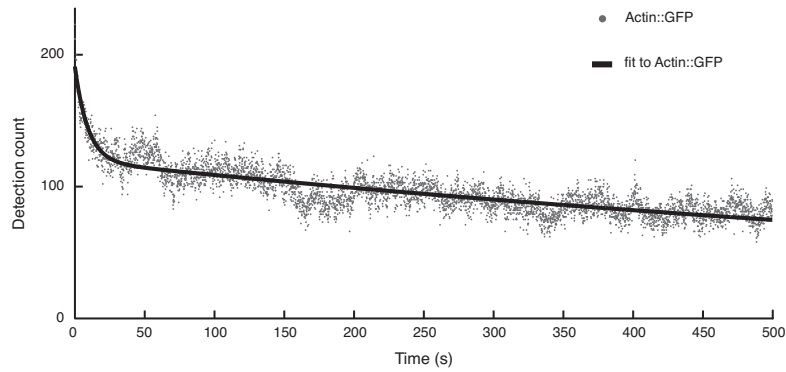
Biphasic response for GFP::Actin under illumination conditions that allow accurate single molecule detection and tracking. Graph shows the actin::GFP count and the corresponding fit to the model. Data is the same as in **Fig. 2c**, with uninterrupted time.

**Supplementary Figure 3.** Tunable and high-density sampling of single molecule behaviors in PAR-6::GFP.
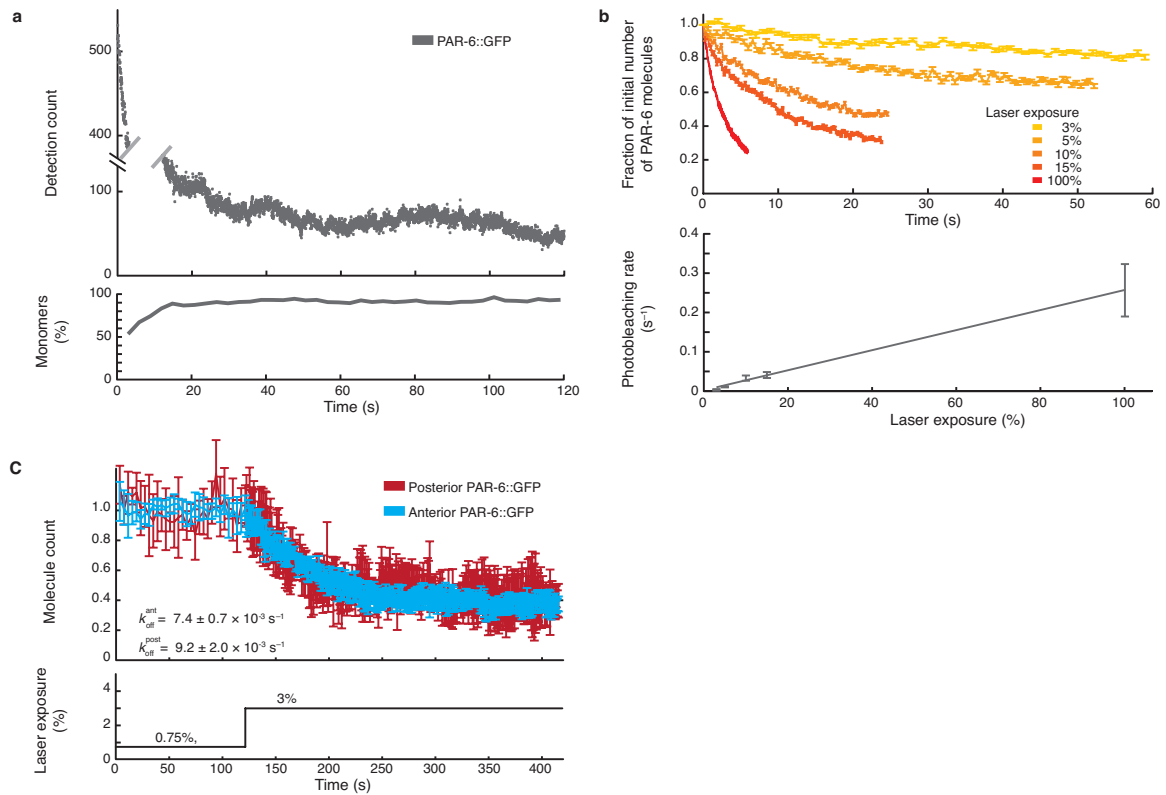
(a) (Top) Biphasic response for PAR-6::GFP under illumination conditions that allow accurate single molecule detection and tracking. (Bottom) Fraction of monomer as a function of time estimated over 100 sequential frames, determined as shown in **Fig. 1f**. Note that an accurate single molecule count for t < 10 s is impossible because only ~50% of the detection events represent single molecules. **(b)** Top: Surface density vs time at various laser exposures, shown as a fraction of the initial unobserved density. Error bars indicate standard error of the mean, (n=10,12,13,11,12, low to high laser). Bottom: Corresponding estimates of per molecule photobleaching (k_{ph}) rate as a function of laser

exposure. Error bars indicate standard deviation. Solid line shows a linear regression against the data. k_{ph} increases linearly with laser exposure. **(c)** Top: Anterior vs posterior densities during an initial weak exposure to laser (left, 0.75%), followed by a 4-fold stronger exposure to laser (right, 3%), showing an initial "unobserved" quasi-steady state, and the equilibration to a new quasi-steady state under "high" laser exposure. Bottom: laser exposure graph. Note that both the anterior and the posterior cortex equilibrate around the same ratio. 100% laser power ~ 1.6 μW.μm^{-2}.

**Supplementary Figure 4.** Analysis of PAR-6::GFP mobility during maintenance phase.
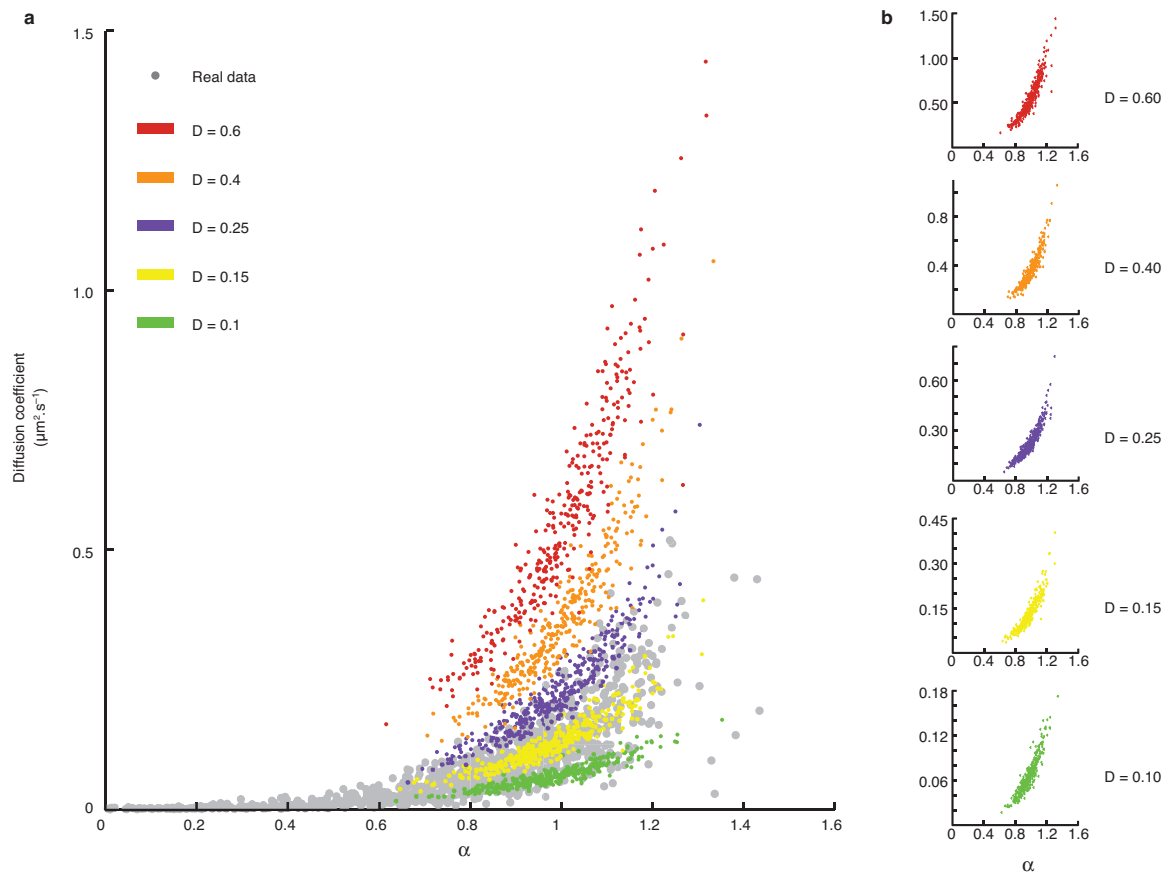
(a) Scatter plot of diffusion coefficient D versus exponent α, measured by fitting $MSD = 4Dt^{\alpha}$ for the first 10 lag times for real data, or simulations of brownian diffusion for $D = 0.1$–0.6 $\mu m^2.s^{-1}$. Note that the best match between simulated and real data is $D = 0.15$, but the cloud of real data points is still wider than simple diffusion with a single diffusion coefficient (see **Supplementary Note 7** for details). **(b)** Increasing the diffusion coefficient only stretches the vertical axis, but for no diffusion coefficient can simulations of brownian diffusion capture the portion of the real data where $D < 0.7$ $\mu m^2.s^{-1}$.

Supplementary Figure 5. Dependence of estimated turnover values on frame averaging and allowable gap size.
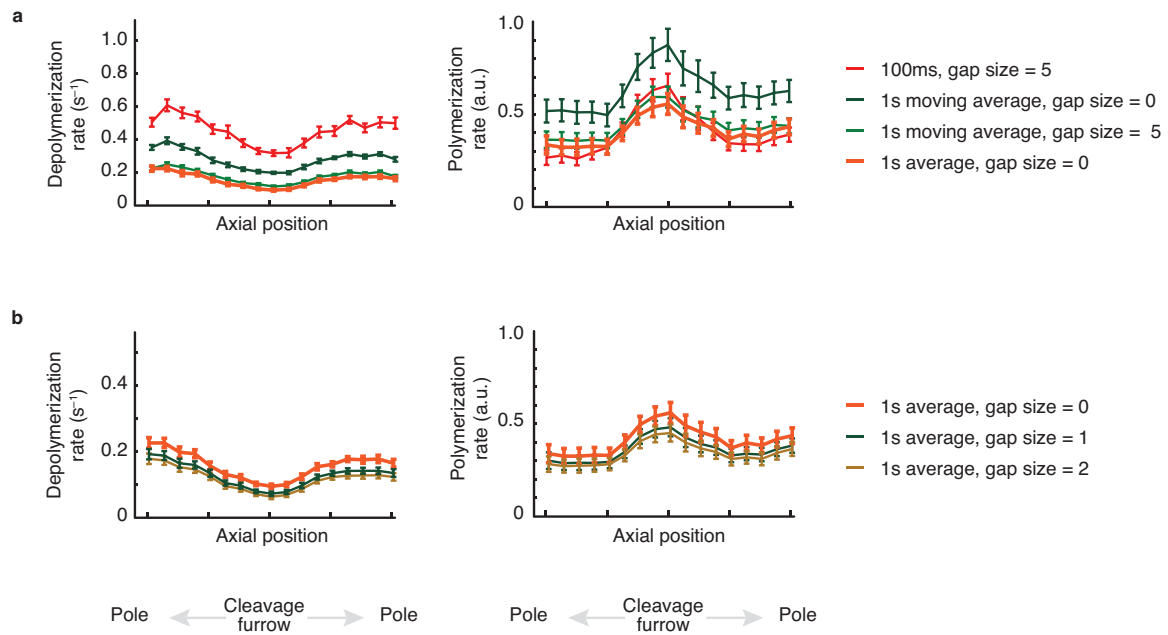
(a) Estimates of assembly and disassembly rates vs axial position during cleavage in a Myosin-depleted embryos for a range of tracking conditions. **(b)** Same data as above; specfic comparison of the 1s average tracked at 1s intervals for gap size = 1–3. The fractional change in estimates of assembly and disassembly rates for different gap sizes is relatively small and is nearly the same for all axial positions, indicating that measurements of relative values should be very insensitive to the small errors caused by disallowing gap closing.

Supplementary Figure 6. Measurement of an upper bound on axial localization precision.
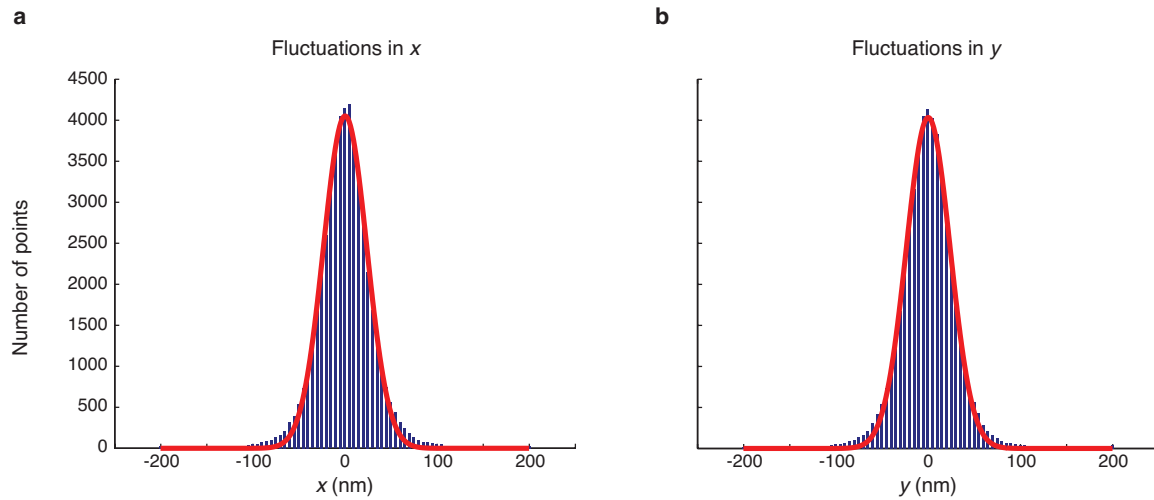
Histograms of positional fluctuations of GFP::Utrophin in embryos arrested during meiosis. Imaging conditions were 100% laser power, 30 ms exposure times as for tracking of PAR-6::GFP. Histograms (blue bars) represent **(a)** x and **(b)** y particle positions for 4784 single molecule trajectories, aligned to the center-of-mass of each trajectory. Gaussian fits to these distributions yield standard deviations of 24 ± 1 nm in x and y. Note that no stage de-drifting was performed on the data.

Table 1. Parameters and statistics for single particle tracking in GFP::Actin and PAR-6::GFP.

Strain	Exposure time (ms)	Laser power (%)	SNR average	SNR 5th percentile	Nearest neighbor average (pixels)	Near. neighb. 5th percentile (pixels)	Step size average (pixels)	Step size 95th percentile (pixels)	Tracklength average (frames)	Tracklength > 80 frames (%)
PAR-6::GFP	30	100	5.4	3.2	40	8.7	0.92	2.3	15	3.6
GFP::Actin	100	30	5.2	2.5	14	5.4	0.49	1.1	37	14.8

Imaging parameters and tracking statistics for accurate single molecule particle detection and tracking in PAR-6::GFP and GFP::Actin strains. Column (1) shows the exposure time, (2) laser power, (3) and (4) average and 5th-percentile of signal-to-noise ratio (SNR), (5) and (6) the average and 5th-percentile of the distance to the nearest particle (in pixels), (7) and (8) the average and 95th-percentile of the frame-to-frame step size (in pixels), (9) the average track length (in frames) and (10) fraction of all tracks longer than 80 frames (in percents). Note that in both conditions, the frame-to-frame step size is much smaller than the distance to the closest particle.

Note 1. smPReSS equations: Measuring turn-over from single molecule loss during photobleaching.

Here we present the kinetic model and fitting procedures that underlie our measurements of photobleaching and turnover rates for GFP-tagged proteins at the cell surface in early *C. elegans* embryos. We consider a population of GFP-tagged proteins that undergo dynamic exchange between a bulk cytoplasmic pool and a patch of the cell surface that is exposed to oblique (near-TIRF) laser illumination. We make the following basic assumptions:

1. The cytoplasmic pool is well mixed

2. The underlying population is kinetically homogeneous; that is the rate constants for local exchange and photobleaching are identical for all molecules

3. The GFP-tagged proteins are representative of the endogenous population; that is they have identical exchange kinetics

4. Photobleaching is restricted to the surface layer, i.e. the photobleaching of cytoplasmic proteins is negligible

5. The diffusive exchange of bleached and unbleached molecules at the edge of the illuminated patch can be neglected.

With these assumptions, we can write a pair of ordinary differential equations that describe the time-evolution of the number of GFP-tagged molecules in the surface patch ($R(t)$) and in the bulk cytoplasm ($Y(t)$):

(1)
$$\frac{dR}{dt} = k_{on} \cdot Y - (k_{off} + k_{ph}) \cdot R$$

$$\frac{dY}{dt} = -k_{on} \cdot Y + k_{off} \cdot R$$

where $k_{on}Y$ is the observable rate (written as k_{app} in the main text) at which molecules appear within the surface patch, $k_{off} =$ is the rate constant for dissociation from the cell surface and k_{ph} is the rate constant for irreversible photobleaching. We use numbers instead of surface density and cytoplasmic concentration to emphasize conservation of mass as molecules flux between pools. In consequence, the parameter k_{on} used here differs from the corresponding k_{on} used in the main text and in **Fig. 2a** by a scale factor equal to the cytoplasmic volume. Note that the values of k_{off} and k_{ph}, the targets of our measurements, do not depend on our choice of units or the size of the GFP tagged pool.

The general solution to equations (1) can be written in the form:

$$R(t) = A_r \cdot e^{r_1 \cdot t} + B_r \cdot e^{r_2 \cdot t}$$

$$Y(t) = A_y \cdot e^{r_1 \cdot t} + B_y \cdot e^{r_2 \cdot t}$$

where

(3)
$$r_1 = \frac{-\sigma - \sqrt{\sigma^2 - 4\kappa}}{2}$$

$$r_2 = \frac{-\sigma + \sqrt{\sigma^2 - 4\kappa}}{2}$$

$$\sigma = k_{on} + k_{off} + k_{ph}$$

$$\kappa = k_{on} \cdot k_{ph}$$

Our primary goal was to extract estimates of k_{off} and k_{ph} by fitting the solution for R(t) to experimental measurements in an initially unobserved cell following a step change in laser illumination. In the solution for $R(t)$, there are 4 parameters to fit, namely r_2, r_1, A_r, B_r. We reduce this to 3 by writing A_r and B_r in terms of k_{ph} and the initial value R(0) as follows:

For $t < 0$ the laser is off; thus $k_{ph} = 0$ and the steady state solution to (1) yields a relationship between initial values $R(0)$ and $Y(0)$:

$$(4) \qquad Y(0) = \frac{k_{off}}{k_{on}} \cdot R(0)$$

For $t > 0$, the laser is on and now we have:

$$(5) \qquad \left(\frac{dR}{dt} \right)_{t=0^+} = k_{on} \cdot Y(0) - (k_{off} + k_{ph}) \cdot R(0)$$

Combining (4) and (5) gives:

$$(6) \qquad \left(\frac{dR}{dt} \right)_{t=0^+} = -k_{ph} \cdot R(0)$$

From (2) and (6), we then have:

$$(7) \qquad A_r + B_r = R(0)$$

$$r_1 \cdot A_r + r_2 \cdot B_r = -k_{ph} \cdot R(0)$$

Solving for A_r and B_r in terms of r_1, r_2 and $R(0)$ and substituting into (2) gives:

(8)
$$R(t) = R(0) \cdot \left(\frac{k_{ph} + r_2}{r_2 - r_1} \cdot e^{r_1 \cdot t} + \frac{k_{ph} + r_1}{r_1 - r_2} \cdot e^{r_2 \cdot t} \right)$$

Fitting (8) to the measured response $R(t)$ yields robust estimates for r_1, r_2 and k_{ph}.
Finally, we can rearrange (3) to obtain:

(9)
$$k_{on} = \frac{r_1 \cdot r_2}{k_{ph}}$$

$$k_{off} = -(r_1 + r_2) - (k_{on} + k_{ph})$$

Note 2: smPReSS experimental procedures

We used a standard MATLAB implementation of non-linear least square curve fitting (lsqcurvefit) to fit equations (8) to measured values for $R(t)$ in defined regions of the embryo surface following a step change in illumination. We extracted standard errors for the fitted values from the fit covariance matrix to estimate the quality of the parameter estimation. In general, these errors (which reflect measurement noise) were negligible when compared to inter-experiment variability. We therefore fit multiple experiments independently and then used the compiled parameter estimates across experiments to estimate parameter means and standard deviations.

A key requirement for obtaining accurate estimates of k_{ph} and k_{off} is that the system must be at its unobserved steady state prior to the onset of illumination. In practice, the illumination required to find and position specimens and fine-tune GFP levels unbalances this steady state and thus once these operations have been achieved it is essential to allow embryos to recover unobserved for a period of time that is significantly greater than k_{off}. For GFP::Actin, which has an estimated lifetime of ~12 s we used a recovery interval of > 30 s. For Par-6, with an estimated lifetime of ~100 s, we allowed at least 180s. In both cases, we obtained similar estimates using longer recovery times.

In addition, it was important that the quasi-steady state value for $R_{qss} \sim \dfrac{k_{off}}{k_{ph} + k_{off}} \cdot R(0)$ is

sufficiently large to avoid counting errors. Thus in practice, we chose imaging conditions such that k_{ph} was comparable in magnitude of k_{off}. For GFP::Actin, this could be achieved under continuous imaging with laser power 30% and 100ms exposure time (**Fig. 4**), or with time-lapse imaging at laser power 100%, 100ms exposure time, for exposures ranging from 12.5% (100 ms exposure every 800 ms) to 100% (continuous exposure) (**Fig. 2**). For PAR-6::GFP, we used an illumination duty ratio of ~3% (1 frame every second, at 100% laser power, 30ms exposure time) to obtain the results presented in **Supplementary Fig. 2c**.

For comparisons of actin turnover, we measured *R(t)* in rectangular regions at the equator or paired rectangular regions at the poles in the same embryos. For anterior vs posterior comparisons of Par-6 turnover in single embryos, we measured *R(t)* in the anterior (resp. posterior) cortex by manually delimiting the regions corresponding to high (resp. low) density in the same embryo. We first fit equation (8) to anterior *R(t)* to estimate k_{ph} and anterior k_{off}. The corresponding measurement for posterior Par-6 was considerably noisier because the posterior density of Par-6 is nearly 10-fold lower than in the anterior, leading to considerably more error in the estimation of k_{off} by curve-fitting. To obtain a more robust comparison, we exploited the fact that with an illumination duty ratio of ~3%, k_{ph} ~ 0.01 s^{-1} and cytoplasmic depletion was negligible; thus R(t) approaches a stable value after ~ 250 seconds of illumination and can be averaged to obtain good estimates of the

quasi-steady state values R_{qss}^{ant} and R_{qss}^{post}. Since $R_{qss} \sim \dfrac{k_{on}}{k_{ph}+k_{off}}$ and $\dfrac{R_{qss}}{R(0)} \sim \dfrac{k_{off}}{k_{ph}+k_{off}}$

when the depletion rate is very small, we could use the measured value of k_{ph} to get good

estimates of k_{off}^{ant} and k_{off}^{post}, and thence k_{on}^{ant} and k_{on}^{post}. The values reported in the text

were obtained by estimating on and off rates for individual embryos and then averaging

the anterior::posterior ratios of these values over 10 embryos.

A key assumption is that the diffusive flux of unbleached GFP from un-illuminated to

illuminated regions of the cell surface could affect our measurements. In the case of

GFP::actin, the mobility is so low that that this is not an issue. For Par-6, given our

estimates of diffusivity $D \sim 0.15$ μm^2.s^{-1} and $k_{off} \sim 0.01$ s^{-1}, we estimate a diffusive

length scale for Par-6 of $L = \sqrt{\dfrac{2D}{k_{off}}} \approx 5$ μm. Thus local flux near the boundary could

influence our measurements. To test this, compared estimates of k_{off} for the entire

anterior region and a smaller subregion obtained by subtracting an outer 3 μm shell

of the original, and measured a small difference of less than 10%. These errors are

systematic and could be corrected, but we chose not to do so here because doing so

would not significantly change the main conclusion of our analysis, namely that

anterior vs posterior differences in k_{off} are small and thus the large (10x) differences

in anterior vs posterior density must be mainly due to differences in recruitment.

Supplementary Video 1. Single molecule movie of PAR-6::GFP. A one cell embryo during maintenance phase expressing PAR-6::GFP at single molecule levels and imaged for 20 s at 30 frames per second, at 100% laser power. Replay speed is 1x. Image size = 331 × 231 pixels, pixel size = 107 nm. Anterior is to the left. Note the range of particle behaviors and mobilities are readily apparent (see main text, and **Supplementary Video 3,4**).

Supplementary Video 2. Single molecule movie of GFP::Actin. A one-cell embryo expressing GFP::Actin at single molecule levels and depleted of NMY-2 by RNAi. The embryo was imaged for 500s at 10 frames per second, at 30% laser power, beginning in maintenance phase and proceeding through anaphase and into telophase. Replay speed is 12x. Image size = 424 × 267 pixels, pixel size = 107nm.

Supplementary Video 3. Single molecule movie of GFP::Actin. Same embryo as in Video 2, showing the entire acquisition sequence. Replay speed is 48x. Image size = 424 × 267 pixels, pixel size = 107 nm. Note that actin is initially evenly distributed along the anterior posterior axis, but during anaphase and telophase, it accumulates at the equator and is depleted from the poles.

Supplementary Video 4. A single PAR-6::GFP molecule displaying simple diffusive behavior. Original image size: 45 × 45 pixels, pixel size: 107nm. Imaging conditions as in **Supplementary Video 1**. Transient failures to detect the particle in a given frame due to motion blur are indicated by the absence of a red circle.

Supplementary Video 5. A single PAR-6::GFP molecule displaying sub-diffusive behavior. Original image size: 45 × 45 pixels, pixel size: 107nm. Imaging conditions as in **Supplementary Video 1**. For this slower moving particle, there are no detection failures.